RSC Advances

PAPER

View Article Online
View Journal | View Issue



Cite this: *RSC Adv.*, 2024, **14**, 28285

# DFT and comparative adsorption study of NiO, MnO, and $Mn_2NiO_4$ nanomaterials for the removal of amaranth dye from synthetic water†

Madiha Ahmad,[a] Qamar Riaz,[a] Mehwish Tabassum,[b] Syed Salman Shafqat,[c] Aima tul Ayesha,[a] Muhammad Zubair,[a] Youpeng Xiong,[b] Asad Syed,[d] Hind A. AL-Shwaiman,[d] Muhammad Arif Nadeem,[ef] Xin Jia,[b] Guobao Xu *[fg] and Muhammad Nadeem Zafar *[af]

In the current study, NiO nanoparticles, MnO nanoparticles, and $Mn_2NiO_4$ nanocomposites (Ni-NPs, Mn-NPs and MN-NCs, respectively) were synthesized using a facile hydrothermal method, and their performance in the removal of amaranth (AM) dye from synthetic wastewater was compared. XRD, FTIR spectroscopy, SEM, BET analysis, and TGA were performed to characterize the produced catalysts. The effect of pertinent parameters, including pH, dosage of catalysts, temperature, and shaking speed on the uptake of AM was investigated through batch experiments. The MN-NCs showed ultrafast and high efficiency for AM removal compared to their counter parts Mn-NPs and Ni-NPs. Under ideal conditions, the highest adsorption efficiencies of AM onto Ni-NPs, Mn-NPs, and MN-NCs were calculated to be 80.50%, 93.85%, and 98.50%, respectively. The Langmuir isotherm fitted the experimental data of AM removal better as shown by the higher values of $r^2$, compared to the Freundlich isotherm, indicating monolayer type adsorption of AM. According to kinetic analyses, the adsorption of AM was best described by the pseudo-second-order kinetic model. Further, regeneration/recycling studies showed that MN-NCs retained 79% adsorption efficiency after four cycles. DFT experiments were also conducted to gain a deeper understanding of the process and behavior of AM adsorption. In conclusion, as Ni-NPs, Mn-NPs, and MN-NCs adsorb AM predominantly *via* electrostatic interaction, they can be applied for the removal of both cationic and anionic dyes by controlling the pH factor.

Received 8th June 2024
Accepted 26th July 2024

DOI: 10.1039/d4ra04208e

rsc.li/rsc-advances



## 1. Introduction

Synthetic dyes are widely produced and used in the food, plastic, textile, and cosmetic sectors. These industries pose serious environmental risks and are considered the main source of water contamination. Dyes are discharged through industrial wastewater into rivers and other water bodies, resulting in harmful effects on aquatic ecosystems and causing proliferation of bacteria and viruses.[1] Dyes are so harmful that they can affect the aquatic environment even at low concentrations.[2] In addition to exerting toxic effects, dyes decrease sunlight penetration and diminish dissolved $O_2$.[3] Among them, azo dyes are more hazardous owing to the existence of toxic amines in the contaminants.[2] Therefore, treating cationic dyes and certain anionic dyes is crucial because of their prevalence in wastewater and the environmental hazards they pose, making their removal a significant concern.[4,5] The adsorption of anionic dyes is often favored under acidic conditions and at higher temperatures, emphasizing the importance of understanding their behavior for effective removal processes.[6] Amaranth (AM) is a luxuriously red, water-soluble dye that is a member of the monoazo group. It is well known that prolonged exposure to/uptake of AM can cause allergy, tumors, birth defects and respiratory problems in human beings;[7,8] hence, different means and ways are needed to remove dyes from wastewaters.

Over the past few decades, several biological, physical, and chemical methods have been investigated for the removal of

[a]Department of Chemistry, University of Gujrat, Gujrat 50700, Pakistan. E-mail: znadeempk@gmail.com; nadeem.zafar@uog.edu.pk
[b]Key Laboratory Incubation Base for Green Processing of Chemical Engineering, School of Chemistry and Chemical Engineering/State, Shihezi University, Shihezi 832003, PR China
[c]Department of Chemistry, Division of Science and Technology, University of Education, Lahore 54770, Pakistan
[d]Department of Botany and Microbiology, College of Science, King Saud University, PO Box 2455, Riyadh 11451, Saudi Arabia
[e]Catalysis and Nanomaterials Lab 27, Department of Chemistry, Quaid-i- Azam University Islamabad, Islamabad 45320, Pakistan
[f]State Key Laboratory of Electroanalytical Chemistry, Changchun Institute of Applied Chemistry, Chinese Academy of Sciences, 5625 Renmin Street, Changchun, 130022, People's Republic of China. E-mail: guobaoxu@ciac.ac.cn
[g]School of Applied Chemistry and Engineering, University of Science and Technology of China, No. 96 Jinzhai Road, Hefei, Anhui, 230026, People's Republic of China

† Electronic supplementary information (ESI) available: Fig. S1–S8, Section S1 and Table S1. See DOI: https://doi.org/10.1039/d4ra04208e

contaminants from water. For such goals, electrochemical techniques have also been employed, along with membrane separation, coagulation, photocatalytic degradation, oxidation, and aerobic/anaerobic microbial degradation.[2,9–11] However, due to the complex aromatic structures of dyes, many dyes possess high resistance to breakdown through conventional treatments, which may result in the transfer of primary pollutants to secondary pollutants, which are more toxic,[8,12] and therefore, they are removed inadequately from contaminated water. There is always a concern in developing effective and lucrative methods for the abatement of dyes from water. Among the several available methods, adsorption has been proposed as the best and dominant alternative method to remove various types of pollutants (dyes, drugs, and metal ions).[13] Activated carbon due to its high adsorption capacity towards different contaminants is among the top adsorbents used at the commercial level but highly expensive.[14,15] This drives the researchers to discover/develop efficient and economical alternative adsorbents, and attempts have been made to identify cost-effective adsorbents for the removal of dyes.[2]

Since the previous few decades, nanomaterials have been intensively explored owing to their tiny size, higher surface area and many other unique qualities.[16–19] Among them, transition metal nanoparticles have been assessed extensively because of their excellent performance in many distinct fields including environment, photocatalysis, and adsorption.[20–25] Their low cost, porous structure, immediate diffusivities, non-toxicity, optical and electronic characteristics, active kinetics and high amplitude make them best alternatives for the adsorption of pollutants.[26,27] Metal nanoparticles are considered universal adsorption agents for ensuring the removal of organic and inorganic contaminants from polluted water, and have been a topic that has excited engineers, scientists, and researchers for several decades.[28–30] In recent years, the widely used method for the production of metal nanoparticles has been the hydrothermal method owing to its numerous advantages such as ease of performance, simplicity, production of highly homogeneous nanoparticles and use of most easily available solvent water.[31] The efficacy of metal nanoparticles to remove contaminants using the adsorption technique is primarily influenced by the pore and particle structure as well as surface area that can be controlled by adjusting the preparation phases involved in synthesis.[8]

Here, we chose to synthesize amorphous transition metal materials (NiO nanoparticles, MnO nanoparticles, and $Mn_2NiO_4$ nanocomposites, abbreviated as Ni-NPs, Mn-NPs, and MN-NCs, respectively) *via* a simple hydrothermal process with cetyltrimethylammonium bromide (CTAB) as a pore and structure directing agent. The produced nanomaterials were physiochemically characterized by X-ray diffraction (XRD), Fourier transform infrared (FTIR) spectroscopy, scanning electron microscopy (SEM), Brunauer–Emmett–Teller (BET) analysis, and thermogravimetric analysis (TGA). Following characterization, the produced Ni-NPs, Mn-NPs, and MN-NCs were used to remove AM from synthetic water. Various adsorption parameters, adsorption isotherms, kinetic models, and thermodynamic models were used to investigate the mechanism of AM adsorption onto Ni-NPs, Mn-NPs, and MN-NCs. The findings of this study may lift the use of amorphous nanomaterials as effective adsorbents.

## 2. Experimental

### 2.1. Reagents and chemicals

Potassium permanganate ($KMnO_4$), urea ($NH_2CONH_2$), nickel chloride hexahydrate ($NiCl_2 \cdot 6H_2O$), hydrochloric acid (HCl), sodium hydroxide (NaOH) and CTAB ($C_{19}H_{42}BrN$) were of analytical grade and obtained from E-Merck (E-Merck, Germany). Amaranth dye (AM) was provided by a local food industry and used as a pollutant in this study. The molecular formula of AM is $C_{20}H_{11}N_2Na_3O_{10}S_3$, and it has a molecular weight of 604.47 g $mol^{-1}$. The pH of the AM solutions was adjusted using buffers, HCl, and NaOH solutions. An AM solution containing nanomaterials was agitated using a horizontal rotary shaker (Wiseshake SHO-2D, Seoul, South Korea).

### 2.2. Preparation of Ni-NPs, Mn-NPs, and MN-NCs

The Ni-NPs were synthesized by a cost-effective and facile hydrothermal method with little modification.[32] For the synthesis of Ni-NPs, a 0.2 M solution of $NiCl_2 \cdot 6H_2O$ was prepared and added drop wise to a 0.1 M solution of CTAB under stirring. A uniform, clear, green solution was obtained by adding 0.1 M urea solution and stirring the mixture for 45 minutes. The solution was transported to an autoclave lined with stainless steel and Teflon and autoclaved at 120 °C for 12 hours followed by cooling to ambient temperature. The separation of green precipitates was achieved by centrifugation of the resulting mixture at 13 000 rpm for 10 minutes. Following centrifugation, the precipitates were obtained by filtration, washed several times with distilled water, and then dried in an electric oven set at 100 °C for 10 hours. The obtained product was ground into a fine powder and the final product were Ni-NPs having a light green hue.

The Mn-NPs were synthesized using the above-mentioned protocol replacing $NiCl_2 \cdot 6H_2O$ with $KMnO_4$ and keeping all other reactants and procedures the same as followed in Ni-NP synthesis. The resulting product was Mn-NPs having a dark brown color. For the synthesis of MN-NCs, both $NiCl_2 \cdot 6H_2O$ and $KMnO_4$ were the starting materials along with CTAB and urea and the same steps were followed as used in Ni-NP and Mn-NP synthesis. The resulting product were MN-NCs of black color.

### 2.3. Characterization

Ni-NPs, Mn-NPs, and MN-NCs were characterized by several methods such as XRD, FTIR spectroscopy, SEM, BET, and TGA. The crystallinity and phase structure of the provided sample were investigated by XRD. Powder XRD spectra for Ni-NPs, Mn-NPs, and MN-NCs were obtained using a PW 3040/60 X'pert Pro X-ray diffractometer (PANalytical, Almelo, The Netherland) incorporating CuK$\alpha$ as the X-ray source operated at 40 mA of tube current and 45 kV of generator voltage. Using KBr pellets and an FTIR spectrometric analyzer (Nicolet 6700 FTIR

spectrometric analyzer), FTIR analysis was performed to identify the different types of functional moieties found in Ni-NPs, Mn-NPs, and MN-NCs. SEM analysis (JSM-6500F, JEOL, Tokyo, Japan) was performed to visually assess the morphology of the Ni-NP, Mn-NP, and MN-NC adsorbents. The measurements of $N_2$-adsorption and desorption were performed using a Micromeritics Tristar 3000 BET analyzer. Prior to analysis, the samples underwent a 10 hours degassing process at 110 °C. The surface area was calculated using the Brunauer–Emmett–Teller (BET) model, the pore size distribution was computed using the Barrett–Joyner–Halenda (BJH) mode, and the pore size was measured using the adsorption/desorption branches of isotherms. A Universal V4.7A TA thermal analyzer was used to study thermal gravimetric (TGA) profiles at 10 K $min^{-1}$ heating rate under continuous flow of air in the temperature range of 0–700 °C.

### 2.4. Adsorption studies

In current investigation, AM from the nearby food sector was ingested without any form of pre-treatment. One gram of AM was carefully dissolved in 1000 mL of double-distilled water (DDW) for producing the stock solution (1000 mg $L^{-1}$). The experimental solutions were generated from this stock solution using a dilution formula. A UV/Visible spectrophotometer (UV3000, Merck, Hamburg, Germany) was used to measure the absorbance of the AM solutions.

Adsorption studies were performed in batch mode to investigate the effect of adsorption factors such as pH (2–12), agitation speed (80–230 rpm), nanomaterial dosage (0.01–0.035 g/0.1 L), temperature (30–60 °C), AM concentration (10–70 mg $L^{-1}$), and contact time (10–70 min) on AM adsorption onto Ni-NPs, Mn-NPs, and MN-NCs. For each experiment, 100 mL of AM solution was agitated in a 250 mL flask with stoichiometric amounts of Ni-NP, Mn-NP, and MN-NC adsorbents under predefined conditions for a specified time period. A horizontal rotary shaker was employed to equilibrate the AM/Ni-NP, AM/Mn-NP, and AM/MN-NC heterogeneous systems. The heterogeneous systems (AM/Ni-NPs, AM/Mn-NPs, and AM/MN-NCs) were subjected to centrifugation and filtration after attaining equilibrium. The remaining AM concentration was determined by measuring the absorbance of filtrate at $\lambda_{max}$ of 521 nm using a UV/Visible spectrophotometer. Using eqn (1), the adsorption capacity, $X_e$ (mg $g^{-1}$), was calculated based on the residual AM concentration:[33]

$$X_e(\text{mg g}^{-1}) = \frac{(C_o - C)V}{w} \quad (1)$$

The removal percentage (%, AM) of AM was calculated using eqn (2):

$$\%, \text{AM} = \frac{(C_o - C)100}{C_o} \quad (2)$$

where $w$ (g) is the mass of the adsorbents (Ni-NPs, Mn-NPs, and MN-NCs), $V$ (L) is the volume of AM solution, $C_o$ (mg $L^{-1}$) is the starting AM concentration, and $C$ (mg $L^{-1}$) is the AM concentration at equilibrium. To figure out the quantity of AM that is being adsorbed, $X_t$ (mg $g^{-1}$) at time '$t$', the parameters $X_e$ and $C$ were substituted by $X_t$ and $C_t$ in eqn (1). The quantity of AM adsorbed and the residual AM concentration at any given time "$t$" are represented by $X_t$ (mg $g^{-1}$) and $C_t$ (mg $L^{-1}$), respectively. All the trials were completed in triplicate and the data were given as mean ± SD.

### 2.5. Reusability study

After the adsorption study, the used MN-NCs containing AM were shaken with 15 mL of a mixture of NaOH (0.01 M) and ethanol to desorb AM from MN-NCs for 30 minutes at room temperature. Afterward, the MN-NCs was separated and washed with deionized water and ethanol to remove any AM left as well as excess NaOH.[34] The obtained MN-NCs were dried at 110 °C and reused again to adsorb AM and this whole process was repeated four times.

## 3. Results and discussion

### 3.1. Characterization of Ni-NPs, Mn-NPs, and MN-NCs

**3.1.1 XRD analysis.** XRD measurements were carried out to analyze the structural phases of Ni-NPs, Mn-NPs, and MN-NCs. The XRD spectrum of Ni-NPs shown in Fig. 1 (black line) revealed the face-centered cubic structure of Ni-NPs.[35] The major characteristic peaks observed for Ni-NPs were centered at 2$\theta$ values of 37.36°, 43.41°, 62.85°, 75.55°, and 79.61° corresponding to the (111), (200), (220), (311), and (222) planes, respectively. The data matched with standard file JCPDS-47-1049, revealing the cubic phase of Ni-NPs. There were no

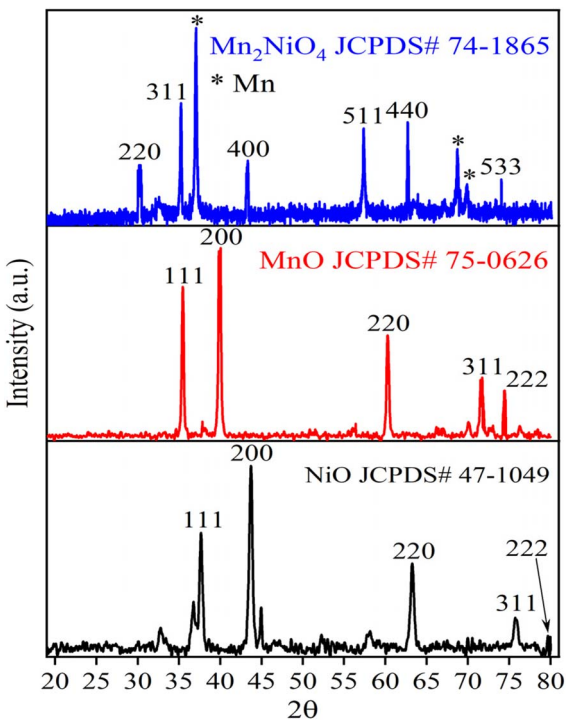


Fig. 1 XRD analysis of Ni-NPs (black), Mn-NPs (red) and MN-NCs (blue).

other peaks observed in the whole spectrum, indicating the purity of Ni-NPs. The characteristic XRD pattern of Mn-NPs (Fig. 1, red line) exhibited certain diffraction peaks having $2\theta$ values of 34.90°, 40.54°, 58.68°, 70.14°, and 73.76° corresponding to the (111), (200), (220), (311), and (222) reflections, respectively.[36] This diffraction peaks indicated that all samples were Mn-NPs with the cubic phase (JCPDS 75-0626). The existence of no additional peak confirmed the purity of Mn-NPs. The XRD pattern of MN-NCs is given in Fig. 1 (blue line). Diffraction peaks at $2\theta$ values of 30.10°, 35.50°, 43.30°, 57.20°, 62.70°, and 74.00° were shown by the MN-NC catalyst and corresponded to the (220), (311), (400), (511), (440), and (533) lattice planes. These values are in good agreement with the spinal phase of $Mn_2NiO_4$ (JCPDS-74-1865).[37] There are some other peaks also observed in the $Mn_2NiO_4$ spectrum, which may belong to some amount of Mn in the sample.

Additionally, it is essential to determine the size and strain of crystallites in materials to gain a comprehensive understanding of their properties and to gain significant insights into the structural features of materials by examining X-ray peak broadening. This analysis enables us to analyze the average size of the crystallites and the strain in the lattice of powder specimens.[38] The structural properties such as crystallite size, strain, and stress of the materials are crucial for understanding the properties and efficiency of the catalysts.[39] After applying various methods such as Debye–Scherrer, Williamson–Hall, Rietveld refinement, and variance, the crystallite sizes of Ni-NPs, Mn-NPs, and MN-NCs were estimated to be 75.6, 55.4, and 28.2 nm respectively and the strain was calculated as 1.76 and 1.44 for Ni-NPs and MN-NCs respectively. The decreasing order of crystallite size can be related to higher adsorption. The micro strain results showed that the decreasing the order, the lesser the deformity in the crystal shape and the higher the adsorption.[40,41] Understanding these factors is crucial for optimizing material properties and predicting strain variations under different loading conditions.[42]

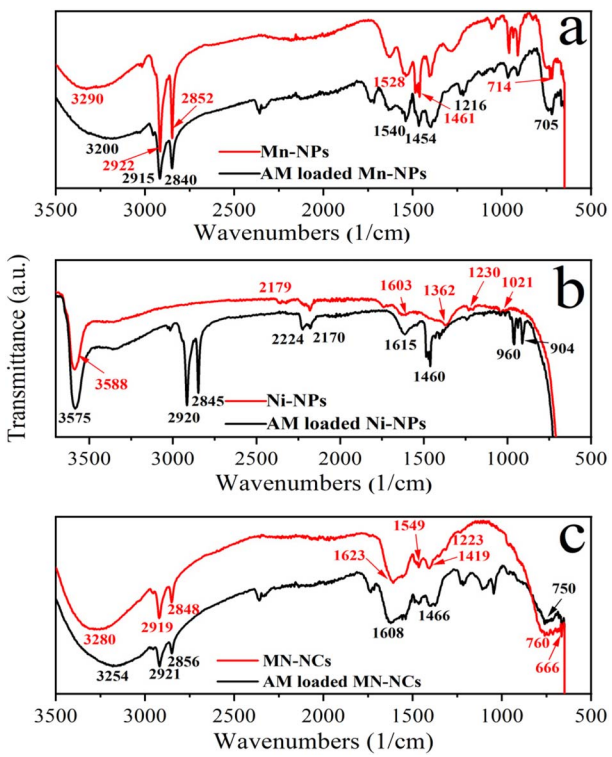


Fig. 2 FTIR analysis of Mn-NPs (a), Ni-NPs (b), and MN-NCs (c) before and after AM adsorption.

**3.1.2 FTIR spectral analysis.** The FTIR spectra of Ni-NPs, Mn-NPs, and MN-NCs before and after AM adsorption shown in Fig. 2 were compared to understand the interaction between AM and functional moieties of fabricated nano-adsorbents. The intense absorption signals observed at 705 $cm^{-1}$ and 904 $cm^{-1}$ were assigned due to the presence of Mn–O bonds (Fig. 2a) and Ni–O bonds (Fig. 2b). The two sharp peaks appearing in the set range of 1400–1620 $cm^{-1}$ were ascribed to the N-related bonds. The presence of the C–H bond was indicated by the two new bands in the range of 2840–2930 $cm^{-1}$. The peaks obtained in 3180–3300 $cm^{-1}$ confirmed the presence of the N–H bond. These observations in shifting of peak values clearly indicate the adsorption of AM over synthesized metal oxides. The adsorption bands at 1525 $cm^{-1}$ and 1600 $cm^{-1}$ attributed to the stretching vibration of the N=N bond. After the adsorption of AM, the FTIR spectra manifested strong signals at 1210 $cm^{-1}$ and 1230 $cm^{-1}$ as the characteristic of the vibrational frequency of the S–C bond. In conclusion, the appearance of new peaks and shifting of peaks in the spectra of Ni-NPs, Mn-NPs, and MN-NCs after AM adsorption, confirmed the successful removal of AM by these nanocatalysts.

**3.1.3 SEM analysis.** The SEM analysis was utilized to examine the morphological aspects of Ni-NPs, Mn-NPs, and MN-NCs, and Fig. 3 presents the SEM images. Fig. 3a presents the SEM images of Ni-NPs, which revealed the porous and cubic morphology. The Ni-NPs appeared to be partially aggregated, which could be due to their high surface energy and exceedingly small size. The images of Mn-NPs were acquired using a scanning electron microscope, which are displayed in Fig. 3b, which indicated the cubic and granular shape of Mn-NPs. The shape of MN-NCs illustrated in Fig. 3c reveals semi spherical/spinal particles with various sizes and inter-planar distances matching the (220) plane, indicating the existence of β-MN-NCs.[43]

**3.1.4 BET analysis.** Through the use of BET analysis, the particular surface area, pore volume, and pore size of the synthesized materials (Ni-NPs, Mn-NPs, and MN-NCs) were identified. MN-NCs exhibited a significantly higher specific surface area than that of Ni-NPs and Mn-NPs, indicating enhanced adsorption properties, which could be attributed to its unique spinel structure and composition. Ni-NPs, Mn-NPs, and MN-NCs displayed type III isotherms with H3 hysteresis loops in the $P/P_0$ range of 0.01–1, as illustrated in Fig. 4. It was observed that at high ($P/P_0$), the isotherms of all samples exhibited an increased uptake of adsorbate, indicating pore filling and the onset of pore condensation. The BET surface area of Ni-NPs, Mn-NPs, and MN-NCs was recorded to be 10.29, 38.57, and 271.8 $m^2\ g^{-1}$, respectively (Table 1). MN-NCs in particular showed a prominent hysteresis in the $P/P_0$ range of 0.4–1, supporting their mesoporous nature; Ni-NPs and Mn-NPs exhibited this characteristic to a considerably lesser extent.

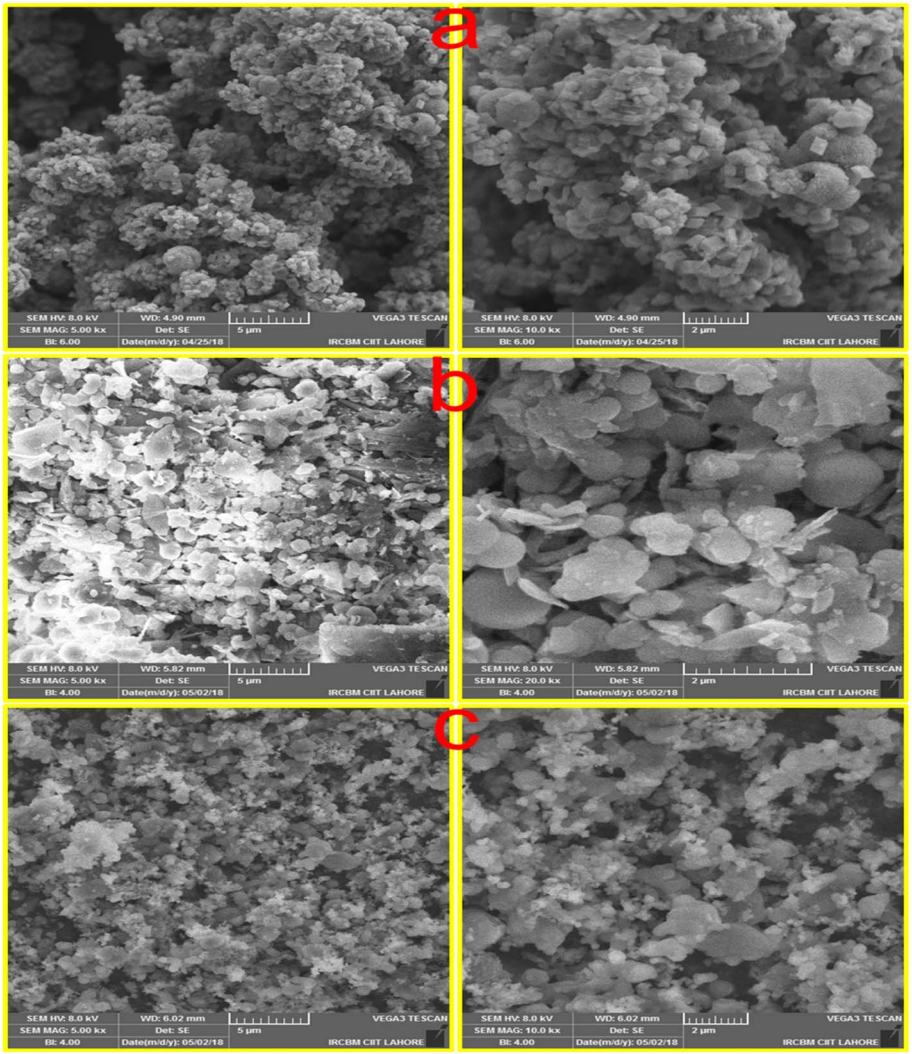


Fig. 3 SEM image of (a) Ni-NPs, (b) Mn-NPs, and (c) MN-NCs.

Most of the pores of MN-NCs were of size 6.827 nm, whereas Ni-NPs and Mn-NPs exhibited pore sizes of 13.07 nm and 17.44 nm respectively. It was also notable that the pore volume of MN-NCs (0.4640 $cm^3 g^{-1}$) was much higher than that of Ni-NPs and Mn-NPs (0.0336 and 0.1682 $cm^3 g^{-1}$ respectively), an aspect that can be of significance in adsorption phenomenon, which requires high pore volume and surface area of materials to provoke a large number of active sites for adsorbates. The maximum adsorption efficacy of AM was calculated to be 80.50%, 93.85%, and 98.50% onto Ni-NPs, Mn-NPs, and MN-NCs, respectively, under optimal conditions. These results are consistent with the BET findings and the results of adsorption experiments of AM over these adsorbents.

**3.1.5 TGA.** To ascertain the thermal properties of Ni-NPs, Mn-NPs and MN-NCs, TGA was performed (Fig. 5). The TGA curve for Ni-NPs exhibited two distinct weight loss regions. The initial weight loss (38.7%) observed between room temperature and 200 °C was linked to the removal of physically adsorbed water molecules and trapped volatile impurities. The second weight loss was characterized by a steep and acceleratory mass decline (39.0% loss) at about 370 °C; the development of the NiO matrix, the evaporation of structural oxygen, and the breakdown of Ni-NPs are all responsible for this peak. After the 2nd step, no noticeable weight loss was observed beyond 400 °C, indicating the formation of Ni-NPs. With regard to Mn-NPs, the TGA curve exhibited stages of weight loss. The initial weight loss (17.6%) that was seen between 45 and 190 °C might be attributed to trapped gasses and water molecules evaporating. The second weight-loss stage (25.3%) between 190 °C and 300 °C corresponds to the evolution of structurally intercalated crystalline water. It was determined that a significant amount of crystalline water, a significant amount of Mn-NPs breakdown loss, the removal of structural oxygen, and the production of MnO matrix were the causes of the third weight loss (9.00%) between 300 and 435 °C.[43,44]

When compared to the individual metal oxide elements, the TGA profile of MN-NCs was less complex and showed two primary phases of weight reduction. The range of 50 to 230 °C accounted for 15.0% of the water molecules that were adsorbed on the samples. The water in a composite system, such as the

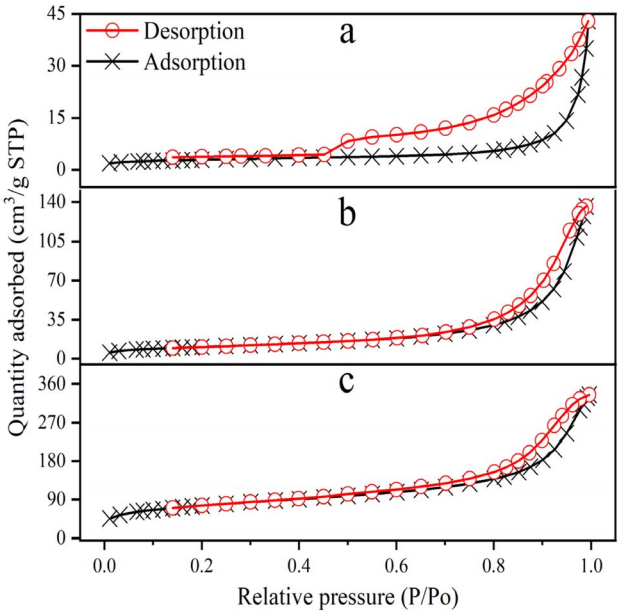


Fig. 4 $N_2$-adsorption/desorption isotherms of (a) Ni-NPs, (b) Mn-NPs, and (c) MN-NCs.

Table 1 BET parameters of Ni-NPs, Mn-NPs, and MN-NCs

| Sample | $S_{BET}$ ($m^2$ $g^{-1}$) | $V_{pore}$ ($cm^3$ $g^{-1}$) | Pore size (nm) |
|---|---|---|---|
| Ni-NPs | 10.29 | 0.0336 | 13.07 |
| Mn-NPs | 38.57 | 0.1682 | 17.44 |
| MN-NCs | 271.8 | 0.4640 | 6.827 |

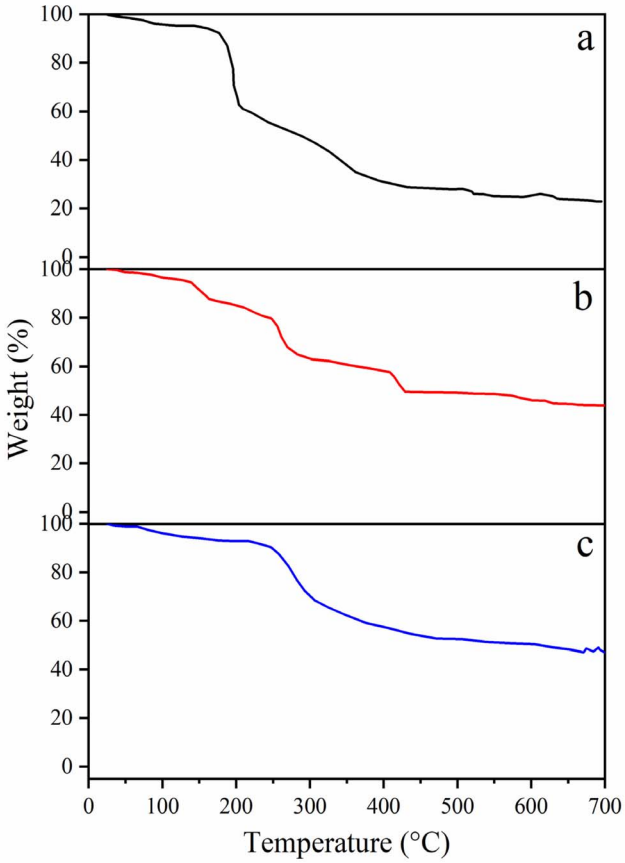


Fig. 5 TGA curves of (a) Ni-NPs, (b) Mn-NPs, and (c) MN-NCs.

binary composite made of MN-NCs used in this work, may be divided into two types: bound water and free water. It takes more heat to extract water from the composite matrix than it does to remove free water. In the region from 250 to 400 °C, decomposition of MN-NCs may occur and removal of structural oxygen, and formation of individual oxides may exhibit.[43]

### 3.2. Effect of adsorption parameters on AM removal

**3.2.1 pH influence.** The pH of the solution has notable effects on the adsorption process as it regulates the ionization state of catalysts and pollutants, which may influence the surface chemistry and active sites of adsorbents. The effect of pH on the adsorptive removal of AM was studied using Ni-NPs, Mn-NPs, and MN-NCs by varying the pH from 2 to 12. Experiment data illustrated in Fig. 6 revealed that Ni-NPs showed the highest AM adsorption at pH 4 while Mn-NPs and MN-NCs significantly adsorbed AM at pH 2. The percentage of AM removal by Ni-NPs was found to be about 89.27 at acidic pH (pH 4) and it dropped gradually to 50.94 at alkaline pH. The percentage of AM removal by Mn-NPs was found to be about 91.15 at acidic pH (pH 2) and it dropped gradually to 60.15 at alkaline pH. A similar trend was observed under the same pH conditions when the AM removal was accomplished with MN-NCs (94.27% at pH 2 and 48.97% at alkaline pH). The decline

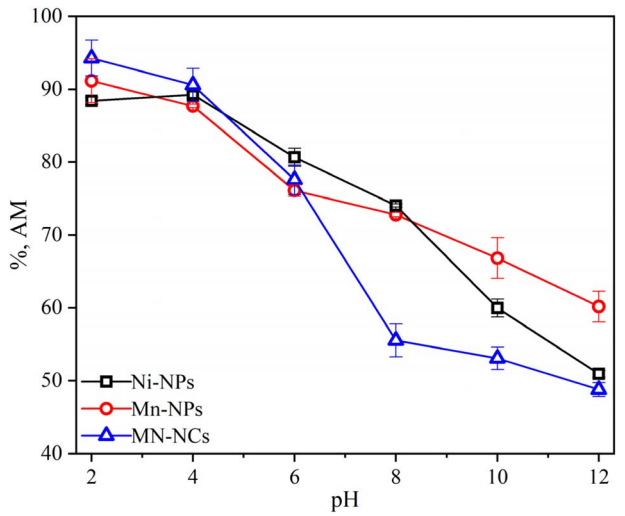


Fig. 6 Effect of pH on the adsorption of AM onto Ni-NPs, Mn-NPs, and MN-NCs.

in dye removal efficiencies with the increase in pH is attributed to the decreased electrostatic interactions between cationic nanoparticles and the negatively charged surface of AM. At low pH, the surface of nanoparticles covered by protons provides more opportunities to adsorb anionic AM dye molecules due to

greater forces of attraction. On the contrary, at a higher pH, the extent of adsorption decreases. This may be attributed to the deprotonation of binding sites of nanoparticles at higher pH values, and hence, the competition between hydroxyl groups and AM anions for binding sites results in a decline in AM adsorption.[45] Furthermore, it can be observed from Fig. 6 that the MN-NCs showed high efficiency in eliminating AM from the solution.

**3.2.2 Shaking speed effect.** At an acidic pH, the impact of shaking speed on AM removal with all nanomaterials (Ni-NPs, Mn-NPs, and MN-NCs) was investigated by adjusting the shaking speed from 75 to 225 rpm at predetermined times (Fig. S1†). Maximum AM removal was 94.02% for Mn-NPs at 150 rpm, and 91.91% and 95.83% for Ni-NPs and MN-NCs, respectively, at 125 rpm. The results show that, when the shaking speed was changed from minimum at 75 to 150 rpm, AM adsorption onto Mn-NPs and Ni-NPs was first enhanced; a further increase in the shaking speed led to a decrease in adsorption efficiency. Such adsorption trend may be explained by the fact that higher shaking speeds at first result in more collisions between pollutants and adsorbent surfaces, which improves the interaction between nanomaterials and AM. At high shaking speeds beyond 150 rpm, AM removal may decrease because AM molecules may be desorbing from the surface of nanomaterials (Mn-NPs and Ni-NPs). However, the adsorption of AM onto MN-NCs was not affected in the whole range of shaking speed and a slight decrease in AM removal from 95.83 to 93.71% was observed when the shaking speed was increased from 125 to 225 rpm.[46] Physical adsorption affects the pore size of the adsorbent surface. The effect of shaking speed on AM removal coincides with that of pore size calculated from BET analysis. The shaking speed directly affects the pore size of the materials. Increasing the shaking speed increases the adsorption while decreasing the pore size of the catalyst.[4] At a higher shaking speed, MN-NCs, specifically, demonstrated a significant hysteresis within the $P/P_0$ range of 0.4–1, indicating their mesoporous nature. Furthermore, Ni-NPs and Mn-NPs showed this property to a much lesser degree and this may be the reason for the high adsorption efficiency of MN-NCs compared to Ni-NPs and Mn-NPs.

**3.2.3 Temperature effect.** The temperature significantly influences the adsorption mechanism, and the effect of temperature (30, 40, 50, and 60 °C) on the removal of AM with Ni-NPs, Mn-NPs, and MN-NCs was investigated, as presented in Fig. S1.† As evident from Fig. S1,† the increase in temperature did not cause any significant effect on the adsorption of AM on all catalysts. The adsorption results depicted that the removal efficiency of AM decreased gradually with the increase in the temperature of solutions for Ni-NPs and Mn-NPs, which might be due to the weakening of interactive forces between AM molecules and the active surface of catalysts at higher temperatures.[47] The decrease in AM removal at higher temperatures may also be related to the increase in the number of random/irregular collisions between adsorbent and adsorbate molecules, which leads to poor adsorption of AM molecules onto nanoparticles. However, the adsorption of AM onto MN-NCs remained almost unaffected or slightly increased when the temperature increases from 30 to 60 °C. Better dispersion of catalyst MN-NCs and more binding sites available at higher temperatures may be the reasons for this behavior.[48] The highest adsorption efficiency of Ni-NPs and Mn-NPs for AM was 95.84 and 96.04% at 30 °C, whereas the adsorption efficiency of AM was 95–97% for MN-NCs at all temperatures.

**3.2.4 Mn-NP, Ni-NP, and MN-NC dosage effect.** The amount of adsorbent (metal nanoparticles) is considered to be the crucial factor that should be adjusted properly to determine the adsorption capacity of adsorbents. Under optimal pH and shaking speed, the effect of Ni-NPs, Mn-NPs, and MN-NCs dosage on the adsorptive removal of AM was studied by adjusting the dose from 0.01 to 0.035 g/0.1 L. Adsorption tests yielded that, at 0.025 g dose, the maximal absorption of AM was determined to be 92.32%, 94.23%, and 96.37% over Mn-NPs, Ni-NPs, and MN-NCs, respectively. First, as in Fig. S2,† the dosage increase from 0.01 g to 0.025 g of adsorbent showed improvement in the % removal of AM. The availability of huge surface area and many active sites can help to clarify this reaction.[23] However, the adsorption efficiency decreased gradually for AM with the further increase in the amount of Ni-NPs, Mn-NPs, and MN-NCs beyond 0.025 g. This behavior is assigned to the fact that a greater number of particles cause congestion as well as agglomeration, which reduces the availability of vacant sites by blocking them and thus resulting in a considerable decrease in adsorption efficiency.

### 3.3. Adsorption isotherms

Using optimal circumstances (pH 2 for Mn-NPs and MN-NCs and 4 for Ni-NPs, dose 0.025 g/0.1 L, room temperature), the influence of AM starting concentration on Ni-NPs, Mn-NPs, and MN-NCs was investigated in order to apply and investigate the adsorption isotherms. Fig. S3† represents the experimental data and from the Figure it can be observed that the retention of AM enhanced with the increase in AM concentration for Ni-NP, Mn-NP, and MN-NC catalysts. There was a linear relationship for all the catalysts between AM removal and starting concentration up to 40 mg $L^{-1}$ AM; beyond that, the increase in AM adsorption was more slow. There are several isothermal models feasible to investigate the adsorption mechanism of contaminants onto nanomaterials. Most often used models are Freundlich and Langmuir.[49,50]

The Langmuir isotherm demonstrates the formation of monolayers on the adsorbent molecules, indicating that the adsorption process is highly specific and occurs in only a limited number of distinct contained sites, showing that the adsorption mechanism is homogenous[51] and mathematically represented using eqn (3):[52]

$$\frac{C}{X_e} = \frac{1}{LX_m} + \frac{C}{X_e} \quad (3)$$

where $L$ is the energy associated with the adsorption process expressed in L $g^{-1}$, $X_e$ is the experimental adsorption capacity expressed in mg $g^{-1}$, $C$ is the AM concentration at equilibrium expressed in mg $L^{-1}$, and $X_m$ is the Langmuir adsorption capacity in the case of homogeneous surfaces. A non-ideal and

Table 2 Adsorption isotherm parameters using Langmuir and Freundlich models for Ni-NPs, Mn-NPs, and MN-NCs

| | | Langmuir | | | Freundlich | | |
|---|---|---|---|---|---|---|---|
| Adsorbent | $X_e$ | $X_m$ | $L$ | $r^2$ | $F$ | $n$ | $r^2$ |
| Ni-NPs | 144.6 | 167.2 | 0.208 | 0.977 | 37.57 | 2.310 | 0.731 |
| Mn-NPs | 160.8 | 168.4 | 0.414 | 0.995 | 54.02 | 2.818 | 0.897 |
| MN-NCs | 167.5 | 172.1 | 0.586 | 0.993 | 69.92 | 3.559 | 0.973 |

reversible mechanism is described by the Freundlich adsorption isotherm involving the multilayer formation on heterogeneous surfaces having different heat, bond energies and affinities for adsorbate species. Mathematically, the Freundlich model is represented by eqn (4):[53]

$$\text{Ln } X_e = \text{Ln } F + \frac{1}{n}\text{Ln } C \quad (4)$$

where $F$ is the Freundlich constant expressed in [mg $g^{-1}$ (mg $L^{-1})^{-1/n}$] and $1/n$ is the factor representing surface heterogeneity or intensity of adsorption. The values of $r^2$, $L$ and $X_m$ were estimated by the linear fitting of Langmuir plot $C/X_e$ *vs.* $C$ (Fig. S4†) whereas $r^2$, $F$ and $n$ were determined by the linear fitting of Freundlich plot Ln $X_e$ *vs.* Ln $C$ (Fig. S5†), and the values of parameters computed from these two isotherms are tabulated in Table 2. The value of $r^2$ (0.9771–0.9953) in the case of Langmuir model were found to be greater as compared to those obtained from the Freundlich model (0.7312–0.9728), and the values of $X_m$ (theoretical) and $X_e$ (experimental) adsorption capacities of AM were approximately close to each other. Both these factors confirmed the suitability of the Langmuir model to explain the AM removal, indicating monolayer adsorption onto the homogeneous surface of all Ni-NP, Mn-NP, and MN-NC catalysts. Additionally, the values of $n$ were in the range of 2.310–3.559, indicating satisfactory adsorption of AM onto Ni-NPs, Mn-NPs, and MN-NCs (favorable adsorption if $n < 10$).

### 3.4. Kinetic modeling

The effect of contact time on the effectiveness of Ni-NPs, Mn-NPs, and MN-NCs in removing AM was planned for different time intervals ranging from 10 to 150 min, keeping all other parameters fixed (pH 2 for Mn-NPs and MN-NCs, and 4 for Ni-NPs, dosage 0.025 g/0.1 L, 40 mg per L AM, room temperature). The goal was to estimate the optimal time desired for the maximum removal of AM by Ni-NPs, Mn-NPs, and MN-NCs. Fig. S6† illustrates the removal of AM at different contact time with Ni-NPs, Mn-NPs, and MN-NCs. The curves in Fig. S6† indicate that the adsorption of AM occurred swiftly at the starting stage followed by a steady increase as the equilibrium was reached. The shape of plots suggested that the available active sites saturated rapidly, especially for MN-NCs, which needed less time to adsorb maximum AM than that of Ni-NPs and Mn-NPs. The maximum adsorption capacity of MN-NCs for AM was observed within 20 min (120 mg $g^{-1}$), whereas Ni-NPs and Mn-NPs achieved maximum removal in 30 min (115 and 119 mg $g^{-1}$ respectively). Further, the equilibrium was reached within 30 min for MN-NCs, whereas for Ni-NPs and Mn-NPs, it was reached in 50 min. Therefore, it can be deducted that the selectivity order to remove AM is MN-NCs > Mn-NPs > Ni-NPs. From the real application point of view, MN-NCs are superior to their counter parts, as longer time may cause higher operational costs.

The mechanism of adsorption process by predicting the adsorbate uptake rate as well as reaction pathways is well explained by studying the kinetics of adsorption process, which can help in modeling a suitable adsorption system. Two well-known models, pseudo-first order (FO) and pseudo-second order (SO), were applied to the adsorption of AM onto Ni-NPs, Mn-NPs, and MN-NCs. The linear forms of pseudo-FO and pseudo-SO are represented using eqn (5) and (6) respectively:[54,55]

$$\text{Log}(X_e - X_t) = \log X_{1e} - \left(\frac{K_{fo}}{2.303}\right)t \quad (5)$$

$$\frac{t}{X_t} = \frac{1}{K_{so}{X_{2e}}^2} - \frac{t}{X_{2e}} \quad (6)$$

where $K_{fo}$ (1 $min^{-1}$) and $K_{so}$ (g $mg^{-1}$ $min^{-1}$) are the rate constants for pseudo-FO and pseudo-SO respectively, whereas $K_{so}{X_{2e}}^2$ is the initial adsorption rate at $t = 0$. The $r^2$, $X_{1e}$, and $K_{fo}$ values were estimated by the linear fitting of pseudo-FO plot $\log(X_e - X_t)$ *vs.* $t$ (Fig. S7a†) whereas $r^2$, $X_{2e}$, and $K_{so}$ were determined by the linear fitting of pseudo-SO plot $t/X_t$ *vs.* $t$ (Fig. S7b†), and the values of parameters computed from these two kinetics models are tabulated in Table 3. The values of $r^2$ (0.6221–0.9072) in the case of pseudo-FO were not close to one as well as there was a huge difference between the theoretical and experimental values of $X_e$, which indicated that the adsorption of AM onto Ni-NPs, Mn-NPs, and MN-NCs did not follow the mechanism of pseudo-FO kinetics. However, the values of $r^2$ (0.9993–0.9999) obtained from pseudo-SO were higher and very close to one, and the theoretical and experimental values of $X_e$ were also in good agreement. Both these factors indicated that the adsorption of AM onto Ni-NPs, Mn-NPs, and MN-NCs followed the adsorption mechanism as per pseudo-SO kinetics, which assumes that electrostatic interaction *via* chemisorption as the monolayer on the catalyst surface may be the rate-limiting step.[56]

To gain further insights into the diffusion mechanism as well as estimation of intraparticle diffusion (IpD) rate constant, the IpD model was applied, which is represented as eqn (7):[57]

$$X_t = K_{ipd}t^{1/2} + C \quad (7)$$

where $K_{ipd}$ (mg $g^{-1}$ $min^{-1/2}$) is the IpD rate constant and intercept $C$ represents the boundary layer thickness.

The values of $K_{ipd}$ and $C$ were determined by IpD plot $X_t$ *vs.* $t^{1/2}$ (Fig. 7), and are tabulated in Table 3. The multilinearity in the plots displayed in Fig. 7 reveals that a two-step diffusion process is involved in the activity of all catalysts ((i) instantaneous adsorption onto the external surface and (ii) IpD). This behavior was also confirmed by the higher values of $K_{ipd}$ in the first step compared to the second step.[56] The AM was initially adsorbed onto the external surface of catalysts with $K_{ipd}$ values 35 times

Table 3 Pseudo-FO kinetic, pseudo-SO kinetic, and IpD model parameters for AM removal using Ni-NPs, Mn-NPs, and MN-NCs

| | Parameters | | | |
|---|---|---|---|---|
| Models | Adsorbents → | Ni-NPs | Mn-NPs | MN-NCs |
| Experimental | $X_e$ (mg g$^{-1}$) | 116.36 | 120.4 | 122.00 |
| Pseudo-FO | $X_{1e}$ (mg g$^{-1}$) | 3.2331 | 2.9914 | 2.1642 |
| | $K_{fo}$ (min$^{-1}$) | −0.0479 | −0.0419 | −0.0267 |
| | $r^2$ | 0.9072 | 0.8714 | 0.6221 |
| Pseudo-SO | $X_{2e}$ (mg g$^{-1}$) | 117.51 | 121.65 | 122.70 |
| | $K_{so}$ (g mg$^{-1}$ min$^{-1}$) | 0.0069 | 0.0066 | 0.0092 |
| | $r^2$ | 0.9994 | 0.9993 | 0.9999 |
| Intraparticle diffusion | 1st region | | | |
| | $K_{ipd}$ (mg g$^{-1}$ min$^{-0.5}$) | 7.2199 | 6.9563 | 11.177 |
| | $C$ | 76.711 | 81.504 | 69.896 |
| | $r^2$ | 0.9112 | 0.9858 | — |
| | 2nd region | | | |
| | $K_{ipd}$ (mg g$^{-1}$ min$^{-0.5}$) | 0.2200 | 0.1993 | 0.1653 |
| | $C$ | 113.79 | 118.11 | 119.91 |
| | $r^2$ | 0.8574 | 0.9356 | 0.9786 |

higher than $K_{ipd}$ of the second step, indicating boundary layer diffusion control adsorption of AM onto Ni-NPs, Mn-NPs, and MN-NCs. It is interesting to note that the $K_{ipd}$ value of first step for MN-NCs was 70 times higher than the $K_{ipd}$ value of the second step, again confirming the fast adsorption of AM onto MN-NCs compared to Ni-NPs and Mn-NPs. Finally based on the IpD model, it is concluded that modulating the rate of AM adsorption involves both IpD and film processes.

### 3.5. Thermodynamic study

To support the feasibility and nature of adsorption of AM onto Ni-NPs, Mn-NPs, and MN-NCs, the estimation of thermodynamic parameters was crucial. Eqn (8) and (9) were used to determine these parameters ($\Delta S$-entropy, $\Delta H$-enthalpy, and $\Delta G$°-free energy change):[58]

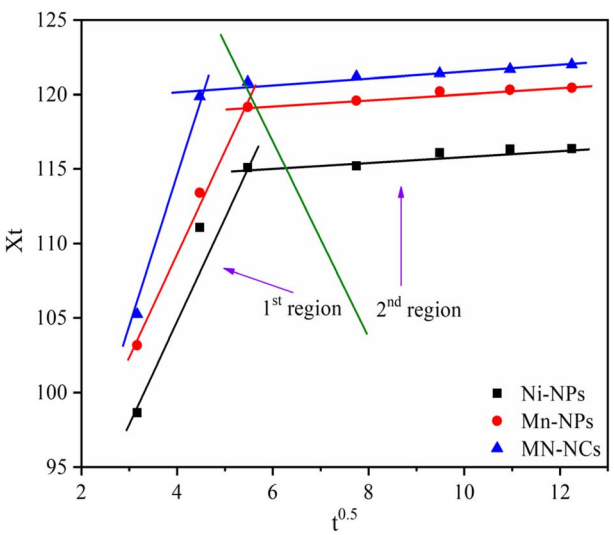


Fig. 7 IpD model for the adsorption of AM onto Ni-NPs, Mn-NPs, and MN-NCs.

$$\Delta G^\circ = \mathrm{RT\,Ln}\,K_{te} \quad (8)$$

$$\mathrm{Ln}\,K_{te} = -\frac{\Delta H}{\mathrm{RT}} + \frac{\Delta S}{R} \quad (9)$$

where $K_{te}$ represents the thermodynamic equilibrium constant. Eqn (8) was used to calculate $\Delta G$°, whereas eqn (9) was used to estimate $\Delta H$ and $\Delta S$. Before computing these parameters, $K_{te}$ was made dimensionless. To make $K_{te}$ dimensionless, the Langmuir constant ($L$) in L mg$^{-1}$ was first transformed to L mol$^{-1}$ *via* the approach described in a previous study[58] using eqn (10):

$$K_{te} = L \times 1000 \times 55.51\ (\mathrm{mol\ L^{-1}}) \times \text{molecular weight of AM} \quad (10)$$

Table 4 shows the estimated values of parameters. Ni-NPs and Mn-NPs had negative $\Delta H$ and $\Delta S$ values, indicating exothermic AM removal, whereas MN-NCs had positive $\Delta H$ and $\Delta S$ values, suggesting endothermic AM removal. The negative $\Delta G$° results indicated that AM removal on Ni-NPs, Mn-NPs, and MN-NCs occurred spontaneously. The $\Delta G$° values ranged from −80 to −400 kJ mol$^{-1}$, indicating chemisorption as the primary mode of AM elimination.[59]

### 3.6. Regeneration and reusability study of MN-NCs

The stability of the adsorbents/materials plays a crucial role in their practical implementation. The MN-NCs were used as the representative adsorbent in the recycling experiment in the

Table 4 Thermodynamics parameters for AM adsorption onto Ni-NPs, Mn-NPs, and MN-NCs

| Parameters | Values | | |
|---|---|---|---|
| Adsorbents | Ni-NPs | Mn-NPs | MN-NCs |
| $\Delta H$ (kJ mol$^{-1}$) | −53.98 | −51.42 | 8.125 |
| $\Delta S$ (J mol$^{-1}$ K$^{-1}$) | −54.66 | −45.24 | 117.6 |
| $\Delta G$° (kJ mol$^{-1}$) | −39.22 | −40.93 | −41.80 |

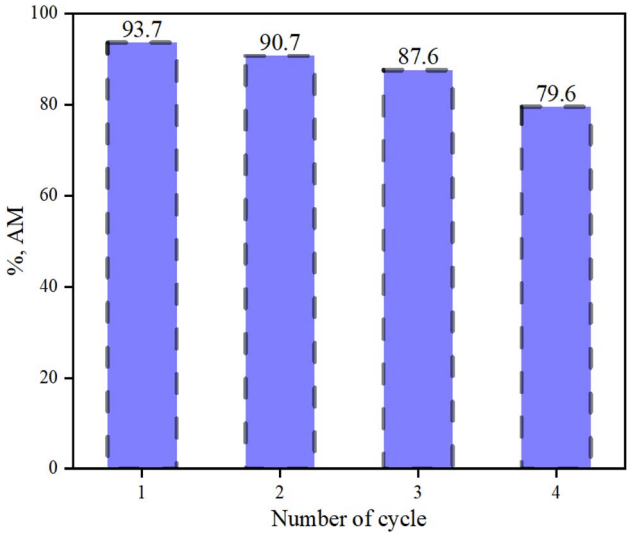


Fig. 8 Recycling of MN-NCs for four cycles to adsorb AM (MN-NC dose 25 mg/0.1 L, AM concentration 40 mg $L^{-1}$, volume of AM solution 100 mL, pH 2).

current investigation. The pH study in Fig. 6 demonstrates that the MN-NCs can adsorb AM (anionic dye) at a pH less than 4, which indicates that the adsorbed AM can be released by controlling the pH.[34] However, the desorption study was performed with a mixture of ethanol/NaOH to improve the desorption efficacy because of the high dissolving ability of organic-based dyes in organic solvents. The results of regeneration and reusability of MN-NCs are represented in Fig. 8, which showed that the MN-NCs retained about 79% of adsorption efficiency after four cycles. Therefore, MN-NCs were found to be readily stable, demonstrating substantial potential of recycling and can be efficiently reused for anionic dye removal.

### 3.7. DFT study

To investigate the mechanism and adsorption pathway of AM removal, DFT was applied to examine the structural properties. DFT methodology is described in Section S1 (ESI data).† AM exhibited the distribution of the lowest unoccupied molecular orbital (LUMO) and highest occupied molecular orbital (HOMO), with the LUMO principally situated on reactive sites C1, N1, C4, C12, and C13, which are accessible electron donors for the reduction reaction. Organic compounds' HOMO and LUMO are commonly employed to explain their oxidation and reduction capacities. However, it is unable to precisely explain the electron gains or losses at each AM molecule location during the process. The electrostatic potential (ESP) mapping displayed that auxochrome groups present in the skeleton of AM were electron-rich active sites. In addition to the charge distribution derived from natural population analysis (NPA), Fig. 9 displays the condensed double descriptor (C5) and the Fukui index. Components C5 with high values of $f$ 0 are more susceptible to free radical attacks ($^{\bullet}OH$ or $^{\bullet}O_2^-$). The condensed dual descriptor (CDD) values were determined based on the $f-$ and $f+$ parameters. The negative values suggested a higher likelihood of electrophilic reactions, whereas the positive values indicated a greater probability of nucleophilic reactions (Table S1†). The highest CDD value of N16 clearly indicated that this is the active site for attacking during the reaction. Orbital 154 was LOMO

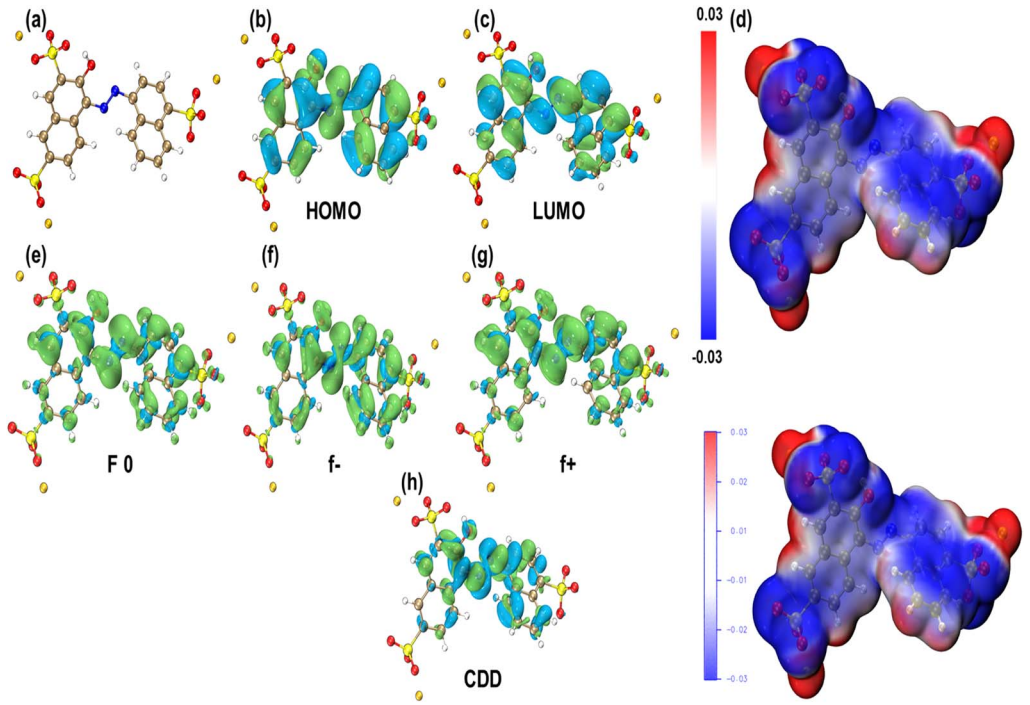


Fig. 9 (a) Chemical structure of AM, (b) HOMO and (c) LUMO distribution on AM, and (d) ESP mapping of AM. The condensed Fukui functions (e) $f$ 0, (f) $f-$, (g) $f+$, and (h) CDD of AM.

Table 5 Comparison of the adsorption capacity of MN-NCs with other nanomaterials reported in the literature

| Adsorbent | Adsorption capacity (mg $g^{-1}$) | Reference |
|---|---|---|
| CTAB-RH | 126 μmol $g^{-1}$ | 60 |
| Magnetic starch | 193.7 | 61 |
| Magnetic $Fe_3O_4$/MIL-88A | 120.3 | 62 |
| Magnetic $Fe_3O_4$/MgO | 37.98 | 8 |
| Iron oxide (Ferrihydrite) | 35.50 | 63 |
| Modified AC | 72.68 | 64 |
| Mt-IL | 263.2 | 65 |
| MN-NCs | 172.1 | This study |

with an energy of −0.098634 a.u. (−2.683962 eV), whereas orbital 153 was HOMO with an energy of −0.212020 a.u. (−5.769348 eV). The LOMO–HOMO gap was calculated to be 0.113386 a.u. (3.085387 eV, 297.694622 kJ $mol^{-1}$). Among all atoms, N16 and N17 displayed more positive CDD values, indicating that they were easily attacked by the catalysts.

Table 5 shows a comparison of AM adsorbed by MN-NCs and other materials reported in the literature. From Table 5, it can be observed that MN-NCs prepared in this study have higher and comparable adsorption capacity in removing AM from aqueous solutions compared to other materials.

### 3.8. Adsorption mechanism

Dye adsorption onto adsorbents/nanoadsorbents can occur *via* physical adsorption or/and chemisorption. In the process of physical adsorption, the dye molecules adhere to the surface of the adsorbent because of van der Waals forces and hydrogen bonding. Chemisorption occurs when dye molecules or ions form a chemical connection with a particular surface functional group or site.[66] The adsorption mechanism is influenced by adsorbent properties including surface area, functional groups, pores, and ideal conditions.[67] The electrostatic attraction and ion exchange may occur between the functional group of AM alongside the protonated interface of the MN-NCs if the mixture is acidic,[68] as shown in Fig. S8.† The possible explanation for the mechanism of AM adsorption on the fabricated adsorbent MN-NCs can be that at lower pH values, the water-metal complex is formed.[69] The hydrogen bonds between negatively charged oxygen on the AM ring and the hydrogen atom present in aqueous nanocomposites facilitate the removal of AM. Alternatively, the formation of a weak pi bond between the electron density of aromatic ring and hydrogen atom in aqueous nanocomposites may be responsible for the adsorption of AM. Other possibilities and routes of mechanism include the adsorption of AM (anionic dye) on the surface of MN-NCs and the formation of intermolecular interaction between the nitrogen and the oxygen of AM with the MN-NC surface.[70] From the kinetic study, the AM adsorption by MN-NCs is assumed to consist of two consecutive steps: (i) transport of AM molecules from bulk solution to the exterior surface of MN-NCs (film diffusion) and (ii) transport of the AM molecules within the pores of the MN-NCs, which occurs on the external surface (IpD or pore diffusion).[71]

## 4. Conclusion

Nano-adsorbents, namely, Ni-NPs, Mn-NPs, and MN-NCs have been synthesized by an environmentally benevolent hydrothermal method and characterized by various techniques to get information on the crystal structure, functional groups, morphology, surface area, pore diameter, *etc.* The nano-adsorbents Ni-NPs, Mn-NPs, and MN-NCs were applied and compared for AM removal from water. Through data analysis, it was established that the adsorption of AM for Mn-NPs and MN-NCs was maximum at low pH 2, while Ni-NPs adsorbed maximum AM at pH 4. The adsorption of AM onto nano-adsorbents Ni-NPs, Mn-NPs, and MN-NCs followed the Langmuir and pseudo-SO models, indicating monolayer adsorption *via* chemisorption. From the thermodynamic study, it was revealed that the removal of AM on MN-NCs was exothermic in nature, whereas endothermic behavior was observed for Ni-NPs and MN-NPs in the removal of AM. The MN-NCs were successfully regenerated and recycled in four consecutive cycles to remove AM. In short, the study showed that these nano-adsorbents may be useful for dye effluent treatment and could help in identifying more efficient nanomaterial types with enhanced qualities for the effective mitigation of pollution.

## Data availability

The authors confirm that the data supporting the findings of this study are available within the article and its ESI.†

## Author contributions

Madiha Ahmad: writing – original draft, methodology, investigation. Qamar Riaz: writing – original draft, investigation. Mehwish Tabassum: formal analysis. Syed Salman Shafqat: software. Aima Tul Ayesha: writing – review & editing. Muhammad Zubair: writing – review & editing. Youpeng Xiong: software. Asad Syed: visualization. Hind A. AL-Shwaiman: funding acquisition. Muhammad Arif Nadeem: validation. Xin Jia: resources, writing – review & editing. Guobao Xu: resources. Muhammad Nadeem Zafar: supervision, conceptualization, project administration.

## Conflicts of interest

The authors declare that they have no known competing financial interests or personal relationships that could have appeared to influence the work reported in this paper.

## Acknowledgements

The authors extend their appreciation to the Researchers Supporting Project number (RSP2024R500), King Saud University Riyadh, Saudi Arabia. We are grateful for financial support from Chinese Academy of Sciences (CAS) President's International

Fellowship Initiative (PIFI) program for Visiting Scientists (Grant No. 2024PVB0003). MNZ acknowledges the CAS for the grant of "President's International Fellowship Initiative (PIFI)" award.

## References

1 R. Kant, *Nat. Sci.*, 2012, **4**, 22–26.
2 M. Blachnio, T. M. Budnyak, A. Derylo-Marczewska, A. W. Marczewski and V. A. Tertykh, *Langmuir*, 2018, **34**, 2258–2273.
3 N. M. Mahmoodi, Z. Hosseinabadi-Farahani and H. Chamani, *Environ. Prog. Sustain. Energy*, 2017, **36**, 111–119.
4 H. Miao, M. Li, X. Sun, J. Xia, Y. Li, J. Li, F. Wang and J. Xu, *Front. Bioeng. Biotechnol.*, 2021, **9**, 827552.
5 S. M. Ibrahim, N. F. Al-Harby, S. A. El-Molla and E. S. Ibrahim, *Sci. Rep.*, 2024, **14**, 14756.
6 A. Strebel, M. Behringer, H. Hilbig, A. Machner and B. Helmreich, *Front. Environ. Eng.*, 2024, **3**, 1347981.
7 A. Basu and G. S. Kumar, *J. Hazard. Mater.*, 2014, **273**, 200–206.
8 A.-N. M. Salem, M. A. Ahmed and M. F. El-Shahat, *J. Mol. Liq.*, 2016, **219**, 780–788.
9 B. Mu and A. Wang, *J. Environ. Chem. Eng.*, 2016, **4**, 1274–1294.
10 I. Bibi, N. Nazar, M. Iqbal, S. Kamal, H. Nawaz, S. Nouren, Y. Safa, K. Jilani, M. Sultan, S. Ata, F. Rehman and M. Abbas, *Adv. Powder Technol.*, 2017, **28**, 2035–2043.
11 I. Shakoor, U. Jabeen, I. Ahmad, S. Riaz, M. Tayyab, A. Syed, A. H. Bahkali, M. Riaz, R. R. Zairov and M. N. Zafar, *Inorg. Chim. Acta*, 2024, **560**, 121837.
12 K. Abdellaoui, I. Pavlovic, M. Bouhent, A. Benhamou and C. Barriga, *Appl. Clay Sci.*, 2017, **143**, 142–150.
13 M. Bashir, M. Batool, N. Arif, M. Tayyab, Y.-J. Zeng and M. N. Zafar, *Coord. Chem. Rev.*, 2023, **492**, 215286.
14 J. E. Aguiar, J. C. A. de Oliveira, P. F. G. Silvino, J. A. Neto, I. J. Silva and S. M. P. Lucena, *Colloids Surf., A*, 2016, **496**, 125–131.
15 H. Sayğılı and F. Güzel, *J. Clean. Prod.*, 2016, **113**, 995–1004.
16 J. Biener, A. Wittstock, T. F. Baumann, J. Weissmüller, M. Bäumer and A. V. Hamza, *Materials*, 2009, **2**, 2404–2428.
17 G. Song, W. Fan, J. Zhang, T. Xue, Y. Shi, Y. Sun and G. Ding, *Appl. Surf. Sci.*, 2024, **661**, 160036.
18 L. Khezami, A. Bessadok, M. Ali Ben Aissa, A. H. Ahmed, A. Modwi, N. Benhamadi and A. Amine Assadi, *Inorg. Chem. Commun.*, 2024, **164**, 112413.
19 N. Dai, X. Liu, L. Yang, X. Huang, D. Song, S. Wang, K. Zhang, X. Liu, W. Dong and Y. Zhang, *Langmuir*, 2024, **40**, 8424–8439.
20 B. Chen, X. Zhao, A. Putkham, K. Hong, E. B. Lobkovsky, E. J. Hurtado, A. J. Fletcher and K. M. Thomas, *J. Am. Chem. Soc.*, 2008, **130**, 6411–6423.
21 L. H. Li, J. Xiao, P. Liu and G. W. Yang, *Sci. Rep.*, 2015, **5**, 9028.
22 M. N. Zafar, M. Amjad, M. Tabassum, I. Ahmad and M. Zubair, *J. Clean. Prod.*, 2018, **199**, 983–994.
23 A. Ghamkhari, L. Mohamadi, S. Kazemzadeh, M. N. Zafar, A. Rahdar and R. Khaksefidi, *Composites, Part B*, 2020, **182**, 107643.
24 S. Kapatel and C. K. Sumesh, *Electron. Mater. Lett.*, 2019, **15**, 119–132.
25 S. Rathod, P. Pataniya, K. K. Joshi, M. Shekh, C. K. Sumesh and S. Kapatel, *Surface. Interfac.*, 2024, **48**, 104216.
26 N. Dhineshbabu, V. Rajendran, N. Nithyavathy and R. Vetumperumal, *Appl. Nanosci.*, 2016, **6**, 933–939.
27 Z. Cui, J. Zhang, Y. Xue and H. Duan, *Langmuir*, 2018, **34**, 3197–3206.
28 M. Roosta, M. Ghaedi, R. Sahraei and M. Purkait, *Mater. Sci. Eng. C*, 2015, **52**, 82–89.
29 R. Manigandan, K. Giribabu, R. Suresh, L. Vijayalakshmi, A. Stephen and V. Narayanan, *Chem. Sci. Trans.*, 2013, **2**, 47–50.
30 H. T. Twinkle, J. Kaushik, A. Sahu, S. K. Chaudhary and S. K. Sonkar, *ACS Sustainable Resour. Manage.*, 2024, **1**, 278–288.
31 H. Hayashi and Y. Hakuta, *Materials*, 2010, **3**, 3794–3817.
32 S. K. Meher, P. Justin and G. Ranga Rao, *Nanoscale*, 2011, **3**, 683–692.
33 S.-F. Lo, S.-Y. Wang, M.-J. Tsai and L.-D. Lin, *Chem. Eng. Res. Des.*, 2012, **90**, 1397–1406.
34 Y.-R. Zhang, P. Su, J. Huang, Q.-R. Wang and B.-X. Zhao, *Chem. Eng. J.*, 2015, **262**, 313–318.
35 R. Goel, R. Jha and C. Ravikant, *J. Phys. Chem. Solids*, 2020, **144**, 109488.
36 S. Chen, Y. Shi, Y. Wang, Y. Shang, W. Xia and H. Y. Yang, *Nanoscale Adv.*, 2019, **1**, 1714–1720.
37 F. Gao, X. Tang, H. Yi, S. Zhao, W. Zhu and Y. Shi, *J. Environ. Sci.*, 2020, **89**, 145–155.
38 R. Manigandan, R. Suresh, K. Giribabu, L. Vijayalakshmi, A. Stephen and V. Narayanan, *AIP Conf. Proc.*, 2014, **1576**, 125–127.
39 V. Honkimaki, and P. Suortti, Effects of instrument function, crystallite size, and strain on reflection profiles, in *Defect and Microstructure Analysis by Diffraction*, Oxford University Press, 2000, Chapter 4, pp. 41–58, DOI: **10.1093/oso/9780198501893.003.0004**.
40 S. Saleem, M. H. Jameel, N. Akhtar, N. Nazir, A. Ali, A. Zaman, A. Rehman, S. Butt, F. Sultana and M. Mushtaq, *Arab. J. Chem.*, 2022, **15**, 103518.
41 K. Desai, S. Alone, S. Wadgane, S. E. Shirsath, K. M. Batoo, A. Imran, E. Raslan, M. Hadi, M. Ijaz and R. Kadam, *Phys. B*, 2021, **614**, 413054.
42 P. Suresh Kumar, L. Korving, K. J. Keesman, M. C. M. van Loosdrecht and G.-J. Witkamp, *Chem. Eng. J.*, 2019, **358**, 160–169.
43 M. B. Rammal and S. Omanovic, *Mater. Chem. Phys.*, 2020, **255**, 123570.
44 S. Ali and M. A. Farrukh, *J. Chin. Chem. Soc.*, 2018, **65**, 276–288.
45 M. A. M. Salleh, D. K. Mahmoud, W. A. W. A. Karim and A. Idris, *Desalination*, 2011, **280**, 1–13.
46 M. E. Argun, S. Dursun, C. Ozdemir and M. Karatas, *J. Hazard. Mater.*, 2007, **141**, 77–85.

47 K. Litefti, M. S. Freire, M. Stitou and J. González-Álvarez, *Sci. Rep.*, 2019, **9**, 16530.
48 M. Arshadi, F. SalimiVahid, J. W. L. Salvacion and M. Soleymanzadeh, *RSC Adv.*, 2014, **4**, 16005–16017.
49 E. Bazrafshan, A. A. Zarei, L. Mohammadi, M. N. Zafar, M. Foroughi, S. Aman, F. Sabri, A. H. Mahvi, F. Barahuie and M. Zafar, *J. Environ. Chem. Eng.*, 2021, **9**, 106570.
50 R. Nadeem, M. N. Zafar, A. Afzal, M. A. Hanif and R. Saeed, *J. Taiwan Inst. Chem. Eng.*, 2014, **45**, 967–972.
51 E. M. Nigri, A. Bhatnagar and S. D. F. Rocha, *J. Clean. Prod.*, 2017, **142**, 3558–3570.
52 I. Langmuir, *J. Am. Chem. Soc.*, 1918, **40**, 1361–1403.
53 H. Freundlich, *J. Phys. Chem.*, 1906, **57**, 384–410.
54 S. Lagergren, *K. Sven. Vetenskapsakad. Handl.*, 1898, **24**, 1–39.
55 Y. S. Ho and G. McKay, *Process Biochem.*, 1999, **34**, 451–465.
56 B. Jamoussi, R. Chakroun, C. Jablaoui and L. Rhazi, *Arab. J. Chem.*, 2020, **13**, 7459–7481.
57 W. J. Weber and J. C. Jr Morris, *J. Sanit. Eng. Div.*, 1963, **89**, 31–60.
58 B. Zafar, S. S. Shafqat, M. N. Zafar, S. Haider, S. H. Sumrra, M. Zubair, N. Alwadai, F. H. Alshammari, A. S. Almuslem and M. S. Akhtar, *Mater. Today Commun.*, 2022, **33**, 104946.
59 S. Dogar, S. Nayab, M. Q. Farooq, A. Said, R. Kamran, H. Duran and B. Yameen, *ACS Omega*, 2020, **5**, 15850–15864.
60 C. Subir, P. Ghosh, M. T. R. Joy, S. Karmaker and T. K. Saha, *Colloid J.*, 2022, **84**, 196–207.
61 J. Tan, L. Kong, J. Fang, X. Liang and Y. Yin, *Environ. Adv.*, 2024, **15**, 100489.
62 Y. Liu, Y. Huang, A. Xiao, H. Qiu and L. Liu, *Nanomaterials*, 2019, **9**, 51.
63 L. Lu, B. Xu, Q. Zhang, T. Lu, U. Farooq, W. Chen, Q. Zhou and Z. Qi, *J. Mol. Liq.*, 2023, **388**, 122766.
64 L. Fu, G. Zhang, S. Wang, L. Zhang and J. Peng, *Appl. Water Sci.*, 2017, **7**, 4247–4254.
65 I. A. Lawal and B. Moodley, *RSC Adv.*, 2015, **5**, 61913–61924.
66 K. B. Tan, M. Vakili, B. A. Horri, P. E. Poh, A. Z. Abdullah and B. Salamatinia, *Sep. Purif. Technol.*, 2015, **150**, 229–242.
67 E. Errais, J. Duplay, M. Elhabiri, M. Khodja, R. Ocampo, R. Baltenweck-Guyot and F. Darragi, *Colloids Surf., A*, 2012, **403**, 69–78.
68 Q. Jing, Z. Yi, D. Lin, L. Zhu and K. Yang, *Water Res.*, 2013, **47**, 4006–4012.
69 N. M. Hosny, I. Gomaa and M. G. Elmahgary, *Appl. Surf. Sci. Adv.*, 2023, **15**, 100395.
70 M. Muslim, A. Ali, S. Kamaal, M. Ahmad, M. J. Alam, Q. I. Rahman and M. Shahid, *J. Mol. Liq.*, 2022, **347**, 117951.
71 Y. Shi, Q. Chang, T. Zhang, G. Song, Y. Sun and G. Ding, *J. Environ. Chem. Eng.*, 2022, **10**, 108639.